Article

Semi-Automatic Detection of Swimming Pools from Aerial High-Resolution Images and LIDAR Data

Borja Rodríguez-Cuenca * and Maria C. Alonso

Department of Physics and Mathematics, Alcalá University, Campus Universitario, Alcalá de Henares, E-28871 Madrid, Spain; E-Mail: mconcepcion.alonso@uah.es

* Author to whom correspondence should be addressed; E-Mail: borja.rodriguezc@edu.uah.es; Tel. +34-918-85-6748.

Abstract: Bodies of water, particularly swimming pools, are land covers of high interest. Their maintenance involves energy costs that authorities must take into consideration. In addition, swimming pools are important water sources for firefighting. However, they also provide a habitat for mosquitoes to breed, potentially posing a serious health threat of mosquito-borne disease. This paper presents a novel semi-automatic method of detecting swimming pools in urban environments from aerial images and LIDAR data. A new index for detecting swimming pools is presented (Normalized Difference Swimming Pools Index) that is combined with three other decision indices using the Dempster–Shafer theory to determine the locations of swimming pools. The proposed method was tested in an urban area of the city of Alcalá de Henares in Madrid, Spain. The method detected all existing swimming pools in the studied area with an overall accuracy of 99.86%, similar to the results obtained by support vector machines (SVM) supervised classification.

Keywords: feature extraction; land cover database; mapping updating; Dempster–Shafer; RAG; NDSPI

1. Introduction

Cartographic feature detection using aerial and satellite images began several decades ago. Detection has changed from being based on visual interpretation [1] to automated or semi-automated detection, in which human knowledge plays a complementary role to classification and decision/detection

algorithms [2]. As time passes, classification algorithms improve, and their accuracy and complexity increases. Several classification algorithms exist and range from very simple, such as minimum distances or Mahalanobis classifiers [3], to more complex, such as maximum likelihood classifiers [3], support vector machines (SVM) [4,5] or neural networks [6]. The latter methods are supervised algorithms; unsupervised algorithms, such as fuzzy clustering [7] or K-means, are useful when no training field is available. Supervised and unsupervised classification algorithms are not fully automatic methods. The current research trend in remote sensing is detecting land cover as automatically as possible [8,9]. Airborne laser sensors and LIDAR have proven to be great advances in land cover detection, complementing aerial and satellite image information. Since the appearance of this data, several works now use LIDAR to detect land covers in terrain. In [10], Song *et al.* presented a land cover classification using intensity and height data provided by a LIDAR flight; Antonarakis *et al.* performed forest and soil-type classification without multispectral images [11]. Both works are based only on LIDAR data. Other works combined aerial/satellite images and LIDAR information to detect different land uses and land covers (LULC). Charaniya *et al.* [12] classified roads, buildings, trees and soil from aerial images, digital elevation models and LIDAR data using a parametric supervised classification algorithm. Building reconstruction fusing aerial images and LIDAR was carried out in [13] by Rottensteiner and Briese. These authors detected buildings using a curvature-based classification.

The method presented in this paper is focused on water body detection, specifically swimming pools located in urban environments. They are land covers of high interest for several reasons, and authorities should have a database with the location of every swimming pool in a region for three purposes. The first reason is to maintain control of taxes and to have knowledge about the energy expenditures involved in maintaining these facilities. Second, the main use of swimming pools is for leisure, but they are an important water source that could be used for firefighting. Wildfires can cause important damages to people and the environment. Rapid detection and suppression of wildfires is key to reducing their destructive effects. Firefighting requires every available resource, and an adequate water supply is critical in a firefighter's arsenal. By utilizing a home's swimming pool, firefighters could have access to strategically placed water supplies. The problem is accurately and quickly identifying which residences have filled swimming pools at the time of the emergency [14]. Producing a database with the location of every swimming pool in a region could be helpful for firefighting [15]. Third, mosquito-borne diseases affect many people throughout the world. Water in swimming pools at unoccupied homes might not be filtered properly, and accumulated rainwater and decomposing leaves likely will not be removed from the pool, providing an ideal habitat for mosquitoes to live and reproduce [16]. The detection of swimming pools, which can provide a habitat for mosquitoes to breed, therefore, is a useful tool in mosquito abatement.

Several works are related to water body detection in open spaces from satellite images. Bo-Cai Gao proposed the Normalized Difference Water Index (NDWI), which provides good results in the detection of open water, such as lakes or rivers [17]. Hanqiu Xu [18] used another index, the Modification of Normalized Difference Water Index (MNDWI), which modifies the latter and provides better results. Zhang *et al.* proposed a method to extract water bodies from satellite images based on entropy, but the results were not satisfactory in small water areas [19]. Frazier and Page [20] detected water bodies on riverine floodplains from Landsat 5 images. Other works carried out flood extent mapping and coastline detection using Synthetic Aperture Radar (SAR) [21–24]. These works

are focused on large water body detection, and they provide good results for this type of land cover. These methods do not provide good results for small-surface bodies of water, such as swimming pools, due to the small size of these bodies and their different spectral response compared with other natural water surfaces [20]. Other works in the current literature present methods oriented toward swimming pool detection. Tien *et al.* [15] carried out swimming pool detection based on a supervised SVM classification applied to an aerial RGB image. The researchers obtained good results in the studied area, but as with every supervised classification method, a previous training field was needed. Galindo *et al.* [25] presented an algorithm to determine the location of swimming pools from a QuickBird image. In this two-step method, swimming pools are first localized in a color analysis phase. Then, the contours of each region identified as a pool are refined using the adjusted object's contour algorithm. This method correctly detected more than 93% of the filled swimming pools in the studied area, failing to identify mostly pools that exhibited occlusion and shadows. Myint *et al.* [26] compared swimming pools and other land cover extraction at the pixel and object levels. To detect swimming pools and water surfaces, they used a segmented QuickBird image and set two thresholds in the second and third component of principal component analysis (PCA). They correctly identified 99% of the swimming pools in the studied area. However, this method is not robust or repeatable, because PCA values change in every image, and the thresholds are not applicable to other images. In [14], Fitzsimmons and Buck presented a method to detect swimming pools from multi-spectral satellite images using the Spectral Angle Mapper (SAM) algorithm. This method provided good results, but requires an accurate training site to work properly, which is not always possible. To identify swimming pools that could serve as mosquito habitats, McFeeters [16] used the NDWI combined with high-resolution multi-spectral imagery and a geographic information system (GIS). This method detected almost 80% of parcels known to have swimming pools. Parcels not identified as containing swimming pools lacked a sufficient amount of surface water to be detected by the NDWI.

This paper presents a semi-automatic methodology to determine the locations of existing swimming pools in an urban environment using aerial images and LIDAR data. The proposed method is based on PCA, image segmentation, a region adjacency graph and the calculation of four decision indices. These indices are combined with the Dempster–Shafer theory to determine the locations of the pools. The results obtained are discussed along with three other methods in order to evaluate the outcomes of the proposed method. This paper is organized as follows. The materials used in the procedure are described in Section 2, and the methodology is discussed in Section 3. The results and the four studied methods are presented in Section 4, and our conclusions are presented in Section 5.

2. Materials

In this document, an aerial image and LIDAR data have been used as input datasets. The aerial image (Figure 1a) was taken by an UltraCam-Xp sensor. Its spatial resolution is 1 meter/pixel, and it is formed by four spectral bands: blue (B), green (G), red (R) and near-infrared (NIR). The image was taken in summer, 2010, in the Spanish city of Alcalá de Henares. The scene used in this paper has a dimension of 400×750 pixels.

LIDAR technology allows the calculation of the digital surface model (DSM) with a precision of the order of 20 cm in planimetry and 30 cm in height [27]. The combination of a sweeping beam laser

with inertial navigation systems and a GPS guarantees high geometric precision in the data. In this study, the LEICA ALS50-II (Leica Geosystems AG, Heerbrugg, Switzerland) sensor to capture the LIDAR data was used. The main features of this sensor are that it works at flight altitudes between 200 and 6000 m, and it has a frequency of 150,000 Hz, a field of view (FOV) between 10 and 75 degrees, a point density up to 150,000 Hz, an altimetry precision of 11 cm, a footprint between 0.3 and 5 m and a point density up to 12 points per square meter. Although a DSM could also be obtained by classical digital photogrammetry, this would be more expensive and slower to produce. The LIDAR data used in the present work correspond to a flight conducted in the summer of 2010. The flight was conducted at an altitude of approximately 1800 m above the ground; the scan angle was ±20 degrees, and the scan frequency 1,000,000 Hz. The resulting point density was 0.5 points per square meter. The coordinate system is WGS84 with orthometric heights.

Figure 1. (**a**) Aerial RGB image; (**b**) digital surface model (DSM); (**c**) intensity LIDAR data; (**d**) near-infrared band from the aerial image; and (**e**) the ground truth made by the authors to determine the accuracy of each studied method.

(a) (b) (c) (d) (e)
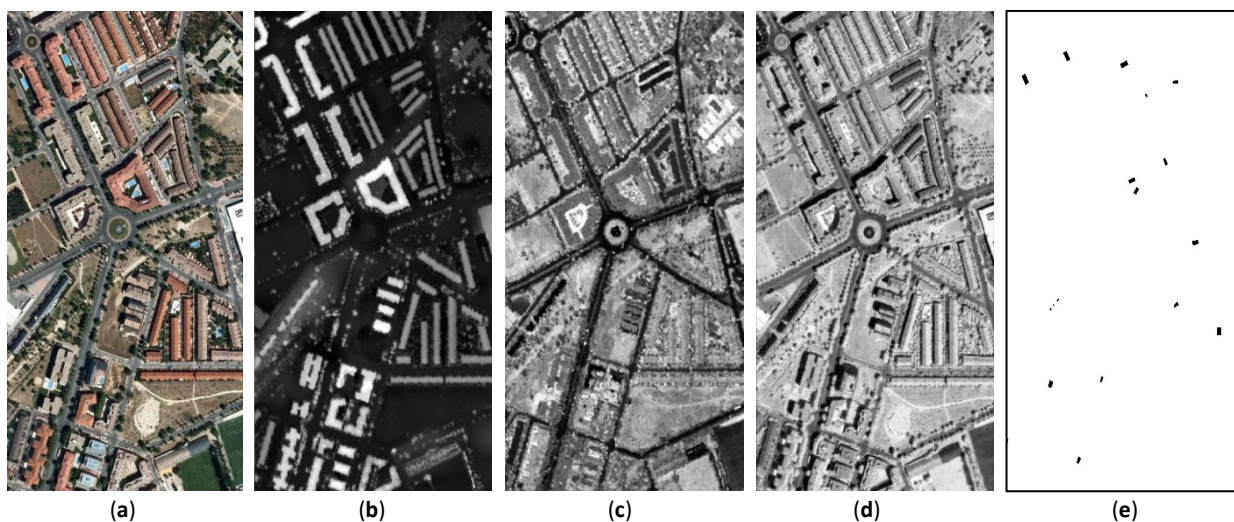
3. Method

In this paper, a method for the semi-automatic detection of swimming pools in urban areas is shown. Identification and extraction begin with the lecture of the aerial image and the rasterization of LIDAR data. Next, segmentation of the aerial image into regions is carried out. The segmented image is used to create a region adjacency graph (RAG), which is useful to manage the image at the region level. Dempster–Shafer evidence theory is applied to determine which category corresponds to each region of the segmented image depending on the value of each studied decision index. The procedure ends with the reassignation of shadowed areas due to a bad behavior of the proposed index to determine the location of swimming pools in these dark regions. Figure 2 shows a flow chart of the method proposed in this paper.

Figure 2. Flow chart of the proposed method for the detection of swimming pools. NIR, near-infrared; PCA, principal component analysis; DSM, digital surface model; DTM, digital terrain model; NDVI, Normalized Difference Vegetation Index; NDSPI, Normalized Difference Swimming Pool Index; RAG, region adjacency graph; nDSM, normalized digital surface model; LULC, land uses and land covers.
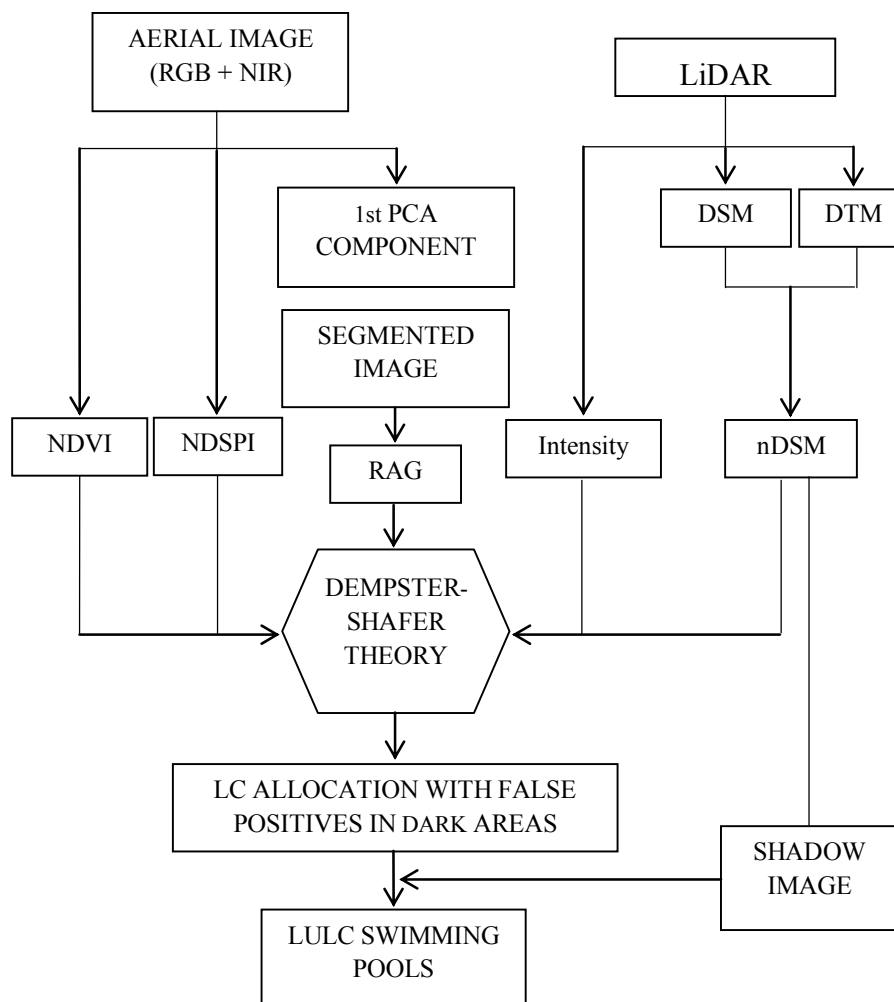
3.1. Aerial Image Loading, LIDAR Data Rasterization and nDSM Generation

The first step in the procedure is reading the different bands involved in the process. Three optical bands (red (R), green (G) and blue (B)) are used from the aerial image, as well as the near-infrared band (NIR).

Height and intensity information was obtained from LIDAR data. The DSM was obtained from the first echo of each pulse after filtering the noise that was generated in the data capture process. The 3D clouds of the LAS file was rasterized using the method proposed by [28], who divided the data into regular cells, with each cell containing a determinate number of individual LIDAR points depending on the local density of each cell. The final elevation for each cell was calculated as the average of several LIDAR points contained within that cell; if a cell was without points, then nearest neighbor interpolation was applied. The cell size was 1 m. The DSM contained information regarding construction, vegetation and uncultivated ground, as seen in Figure 1b. The digital terrain model

(DTM) was generated as a product derived from the DSM after employing a semi-automatic method developed by [29]. This method consists of applying several filters to the DSM with the intention of removing the non-ground points. Next, minimal manual editing of the points that had not been properly classified was necessary. Finally, the normalized digital surface model (nDSM) was generated by calculating the difference between the DSM and DTM. LIDAR data come in a binary format according to the ASPRS norm. The LAS format includes information, such as GPS time and intensity, in addition to echoes of the pulses. In addition to height, intensity data was rasterized to add information to the process. The final intensity value of each pixel was calculated as the average of all intensity values of the LIDAR points contained in each cell, as in the rasterization of height data. The rasterization of DSM and intensity data are shown in Figure 1b,c, respectively. The near-infrared band of the aerial image is shown in Figure 1d.

3.2. Segmentation of First Component Image from PCA

Segmenting an image involves moving from the pixel-level to the segment-level in order to reduce its dimensionality. Segmentation involves group pixels that have similar properties; these pixels are treated as a set. Several methods for segmenting exist, such as clustering [30], thresholding [31] or region-growing [32]. A recent review of existing segmentation methods can be seen in [33]. In the work presented in this paper, region-growing segmentation was carried out [34].

A region-growing method is applied to a single band. Images used in this work are composed of several bands. To consider a single band, a principal component analysis (PCA) was applied to the four bands of the aerial image. Only the first component of PCA, which is the one with the most information, was considered. The first PCA component and the seeds from which the regions grow are the inputs of the region-growing method. Several ways to consider the seeds are present (randomly, consecutively, *etc.*). The present work considers as seeds every pixel that in a pass from left to right and from top to bottom of the first PCA component does not yet belong to any region. The process begins by taking as the first seed the pixel in the top left corner of the image. In the first step, the region is composed of the seed, and this region grows iteratively by comparing the seed with each neighboring pixel. The neighborhood for the studied pixel (i,j) is considered those pixels that share at least one edge. A predetermined threshold (α in Equation (1)) discriminates between the membership and non-membership of a pixel in a region. In a region of n pixels, the studied pixel (i,j) is assigned to this region if the difference between the digital value (DV) of the pixel and the mean DV of the studied region is lower than the threshold (1). Otherwise, the studied pixel is not assigned to the region, and it is considered a seed in the next step of the procedure. Subsequently, the next pixel that does not belong to any region is considered a seed. If a pixel is assigned to a region, it is not considered a seed in this procedure. The region-growing method ends when all pixels in the image are assigned to a region [35–37].

$$\frac{\sum_{k=1}^{n} DV_k}{n} - \alpha < First\ PCA\ component[i,j] < \frac{\sum_{k=1}^{n} DV_k}{n} + \alpha \qquad (1)$$

3.3. Creation of a Region Adjacency Graph (RAG)

A region adjacency graph (RAG) is a type of data structure that facilitates merging and splitting operations. In this work, the RAG was used to represent regions contained in an image and the

relationship between them. Every node of the graph represents a region of the segmented image and contains its information. The edges are used to represent the connection between regions; edges link nodes that represent neighbor regions (see Figure 3). RAG is useful for emphasizing region adjacency and plays an important role in index calculation and assigning coverage.

Figure 3. (**a**) Synthetic image formed by nine regions and fifteen edges; and (**b**) corresponding region adjacency graph (RAG).

(a)   (b)
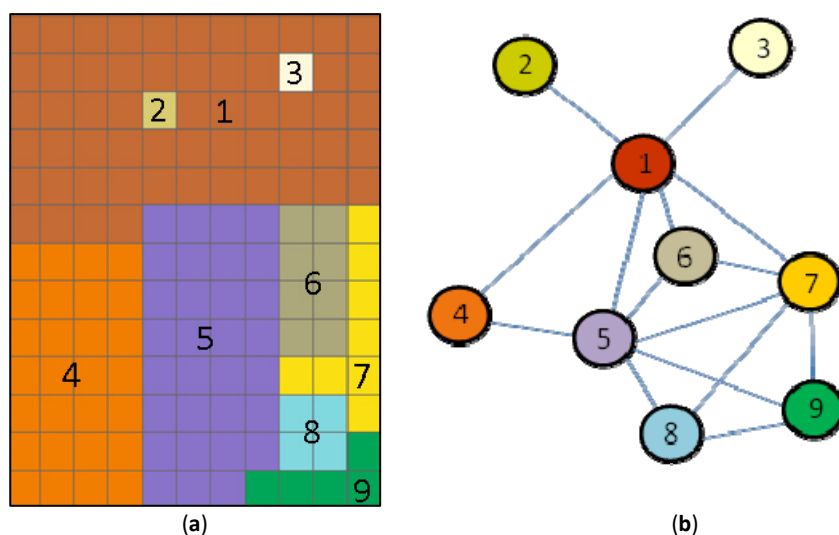
3.4. Decision Indices Computing

Even though the final result is a binary image that only represents swimming pools and background, five types of land covers were considered in the beginning of the procedure: vegetation, buildings, roads, bare soil and water bodies. Better results were obtained by increasing the number of classes. If only two classes are considered, there would be a class that includes elements of a very different nature. This would produce errors in the detection of land covers. Four decision indexes were used for the detection of the five land covers: the Normalized Difference Vegetation Index (NDVI), LIDAR intensity the nDSM and the index created by the authors of this work, aimed at detecting pools, the Normalized Difference Swimming Pool Index (NDSPI).

3.4.1. NDVI

The NDVI index was used to detect the location of vegetation land cover. The use of this index is very common in remote sensing applications to estimate the quality, quantity and development of vegetation from aerial or satellite images. The NDVI index has been used to, among other applications, monitor global vegetation [38] and crop growth [39] or to conduct deforestation studies [40]. The spectral response of vegetation has a characteristic shape with radiance in the near-infrared wavelength (NIR), much higher than in the bands of the visible spectrum, where it takes the lowest values in the blue (B) and red bands (R). No other categories considered have a spectral signature of these features. The NDVI index combines the information from the red and NIR bands to determine the location of vegetation (2) (see Figure 4a).

$$NDVI = \frac{NIR - RED}{NIR + RED} \tag{2}$$

3.4.2. LIDAR Intensity

LIDAR data not only provides a surface digital model, but offers other data, such as the image of the point density or the intensity of the reflected laser pulse at the surface. Asphalted surfaces provide small LIDAR intensity values [41]. This characteristic of the laser pulse intensity LIDAR has been used to detect roads in the image (see Figure 4b). Since a building may have a similar spectral response to an asphalted region, LIDAR intensity has been combined with nDSM to avoid false positives. Thus, only regions with low intensity values and low heights will be considered as roads.

3.4.3. nDSM

In order to detect high elements, an nDSM has been used. The nDSM was obtained from a DSM provided by LIDAR data and a DTM generated as a product derived from the DSM. The nDSM was generated by the research group to which the authors of this work belong [29] (see Figure 4c). The aerial images and the nDSM are geo-referenced properly and have the same spatial resolution, making it possible to combine and work with them at the same time.

3.4.4. NDSPI

Open water surfaces (oceans, rivers, lakes, *etc.*) have a characteristic spectral signature. The highest reflectance of these covers in the electromagnetic spectrum occurs in the blue wavelengths (0.45 to 0.47 μm) and the greatest absorption in the infrared wavelengths (0.7 to 300 μm). Figure 5 shows the spectral response of three sheets of open water. This dataset has been obtained from aerial images from different parts of Spain. The highest reflectance is obtained in the wavelengths corresponding to blue, except for Lake 2, in which the highest reflectivity occurs in the green wavelengths, but is close to the blue band. The lower reflectance occurs at the wavelengths corresponding to the NIR wavelengths. It has been observed that the spectral response of swimming pools is quite different to other sheets of open water. These differences may be due to the properties of pool water and the background color of these elements. It was observed that higher reflectance is retained in wavelengths corresponding to blue. However, the lowest reflectance takes place in the red band, instead of in the NIR wavelengths, as happened in the open water surfaces (see Figure 6)

Taking advantage of this characteristic of the spectral signature of swimming pools, the authors of this paper have developed an index to detect this land cover. This index is derived from the red (R) and blue band (B) (3) of the visible spectrum:

$$NDSPI = \frac{BLUE - RED}{BLUE + RED} \tag{3}$$

The latter index provides the highest values in swimming pools and shadowed regions. These false positives in the dark areas are corrected by generating an image of the shadows, as explained below (see Figure 4d).

Figure 4. (**a**) NDVI index image; (**b**) LIDAR intensity; (**c**) nDSM; and (**d**) the NDSPI index created by the authors.

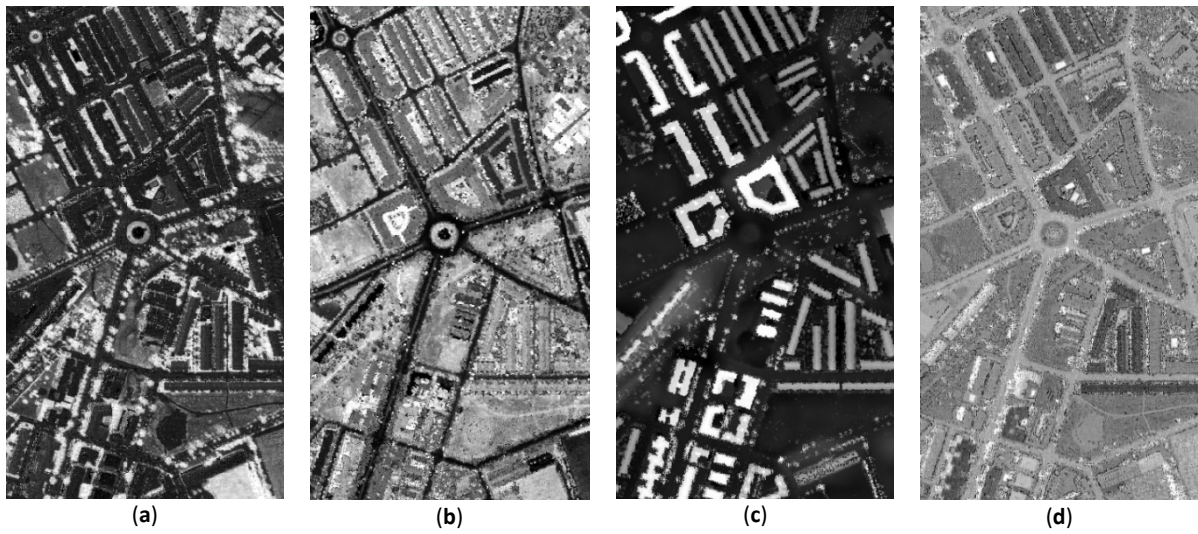(**a**)   (**b**)   (**c**)   (**d**)

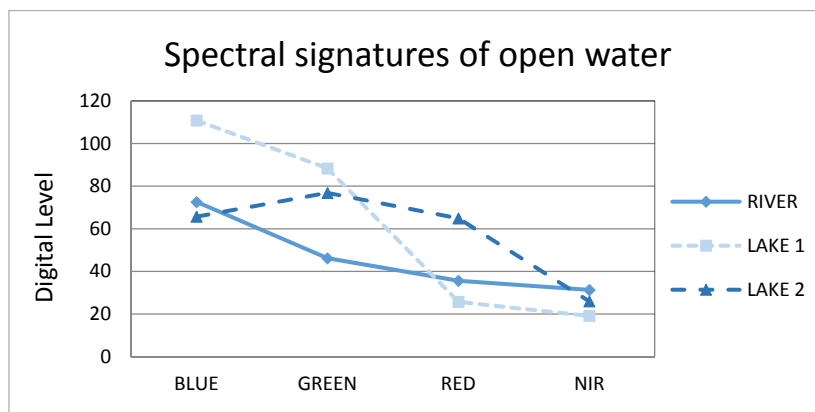**Figure 5.** Spectral signatures of a river and two lakes in an aerial RGB-NIR image.
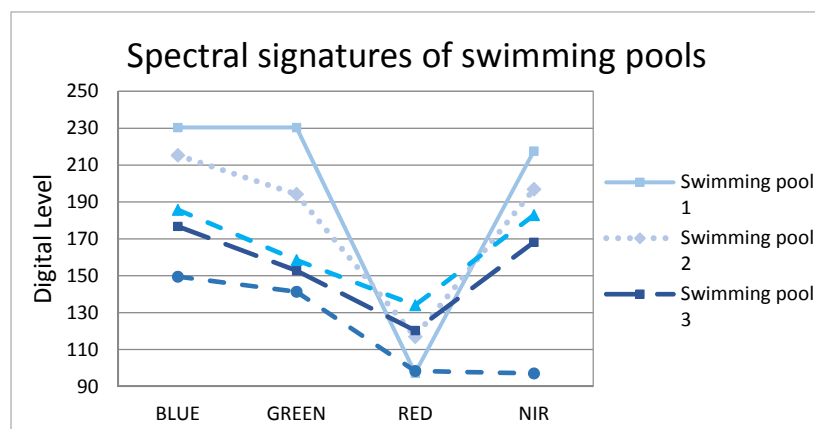

Figure 6. Spectral signatures of five swimming pools in an aerial RGB-NIR image.

3.4.5. NDWI

To test the efficiency of the proposed NDSPI and to determine which index has the highest accuracy, the NDWI (4) used in other works to determine the location of water bodies [42] was included in the procedure. For water extraction, NDWI was adopted and defined as:

$$NDWI = \frac{GREEN - NIR}{GREEN + NIR} \tag{4}$$

in which *GREEN* and *NIR* represent the green band and the near-infrared band, respectively. This index was designed to maximize reflectance of water by using green wavelengths, to minimize the low reflectance of NIR by water features and to take advantage of the high reflectance of NIR by vegetation and soil features. Thus, water features have positive values, while vegetation and soil have negative values.

3.5. Dempster–Shafer Theory

Evidence theory was developed by Dempster [43] and was later extended by Shafer [44]. For this reason, it is commonly referred to as the Dempster–Shafer theory. The objective of this theory is to model the way in which humans assign evidence to different propositions [45]. Evidence theory can be considered as a special case of fuzzy theory [46]. It is motivated by the difficulties found in the theory of probability, representing uncertainty. With the advent of the computational capacity of computers in the 1960s, it became necessary to create theories to model human thought. Classical logic and mathematics had very rigid models for this new phenomenon of scientific interest: the uncertainty that develops every human activity. Zadeh [47] was the first to propose and develop the theory of fuzzy sets.

The mathematical theory of evidence is a field in which data sources are treated separately, and their contributions are combined to provide a joint inference on the correct label for every pixel. Although evidence theory involves the numerical manipulation of quantitative measures of the test, the link between these measures and the original dataset is left to the user. This theory does not require a full probability model against the requirements of other approaches. It attempts to benefit from the use of sets of assumption hypotheses rather than separate hypotheses, as other approaches do. It aims to facilitate the reallocation of belief in hypotheses when evidence changes. It attempts to model the decrease of a working set of hypotheses from evidence accumulation [3].

3.5.1. Dempster–Shafer Theory in Land Cover Detection

The objective of the work presented in this paper is to generate a map with the location of five land covers in the studied area. The ultimate result is to detect only swimming pools, but five categories are taken into account: buildings, vegetation, roads, bare soil and pools. In the Dempster–Shafer theory, the building class is noted with X and vegetation with Y; Z corresponds to roads, T bare soil and W swimming pools. Also considered is θ as the inherent uncertainty in the theory of evidence. The frame of discernment, Ω, is formed by X, Y, Z, T, W and θ:

$$\Omega = \{X, Y, Z, T, W, \theta\}$$

For each decision index, the mass of evidence is noted by μi (i = 1…4, the number of decision indices considered): ($\mu_i(X)$, $\mu_i(Y)$, $\mu_i(Z)$, $\mu_i(T)$, $\mu_i(W)$, $\mu_i(\theta)$), with the assumption that $\mu_i(X) + \mu_i(Y) + \mu_i(Z) + \mu_i(T) + \mu_i(W) + \mu_i(\theta) = 1$, , $\forall i = 1… 4$ [48]. The probability of belonging to each category ($\mu_i(X)$, $\mu_i(Y)$, $\mu_i(Z)$, $\mu_i(T)$, $\mu_i(W)$, $\mu_i(\theta)$) is determined from the values taken by each index on every region according to some functions developed by the authors. Thus, a high NDVI value corresponds to a high probability of belonging to vegetation land cover and a low probability of belonging to the remaining land cover.

With the values, $\mu_i(X)$, $\mu_i(Y)$, $\mu_i(Z)$, $\mu_i(T)$, $\mu_i(W)$, $\mu_i(\theta)$, for the four decision indices (i = 1…4), the evidence combination rule of Dempster–Shafer is applied for every region in the image [43]. This combination (μ_{ij}) is an iterative process in which the knowledge acquired with a certain rate (μ_i) is combined with the following index (μ_j) Equation (5):

$$\mu_{ij} = (\mu_i \otimes \mu_j)(A) = \frac{\sum_{B\cap C=A} \mu_i(B)\,\mu_j(C)}{\sum_{B\cap C \neq \varnothing} \mu_i(B)\mu_j(C)} \tag{5}$$

The result of this process is, for every region, the probability of belonging to each of the considered categories.

3.5.2. Land Cover Allocation

Once the RAG was generated and the Dempster–Shafer evidence theory was applied, land cover allocation was carried out. As discussed in the previous section, the result of applying Dempster–Shafer to each region in the segmented image was the probability of belonging to each of the five categories. According to the Dempster–Shafer results, each region was assigned to the category to which it had the highest probability of belonging. Until this point, five categories have been taken into account, but at this point, they are reduced to two: swimming pools and background. Background land cover includes vegetation, buildings, bare soil and roads. The results of land cover assignment provide false positives in shadowed regions; some dark regions are labeled as water bodies. Figure 7 shows the regions detected as swimming pools after the land cover allocation based on probabilities obtained with the Dempster–Shafer theory.

3.6. Shadow Detection and Correction of Dark Regions Labeled As Water Surfaces

As seen in Figure 7, after the land cover allocation based on probabilities obtained with the Dempster–Shafer theory, several regions are labeled as pools that belong to other land covers.

This is because the spectral response of shadowed regions provides reflectance values in the red wavelengths lower than those that correspond to blue wavelengths (Figure 8). This property shows that some shadowed areas have a similar value on the NDSPI index as swimming pools. To correct this error, a reallocation of coverage in the shadowed regions that have been labeled as sheets of water is carried out. This is achieved by generating a shadow image from the flight data from which the image was taken. The shadow image is generated using an algorithm developed by our research group [49]. By combining this image and the RAG, it is possible to determine the regions that were in a shadowed area and were labeled as sheets of water. Those regions are assigned to the next category with the highest probability, different from swimming pools, according to the Dempster–Shafer results.

Furthermore, a minimum size of four square meters has been set for swimming pools, because pools under that size are not in consideration. Regions labeled as sheets of water that are less than 4 pixels have been assigned to other categories, as well (Figure 9).

Figure 7. (**a**) The detail of the studied area in RGB; (**b**) swimming pools detected in the former detail (it is possible to see two swimming pools correctly detected and two large false positive regions in dark areas); (**c**) another detailed imaged of the studied area in RGB; and (**d**) swimming pool detection (there are no pools in this area, but there are some false positives in shadowed regions).
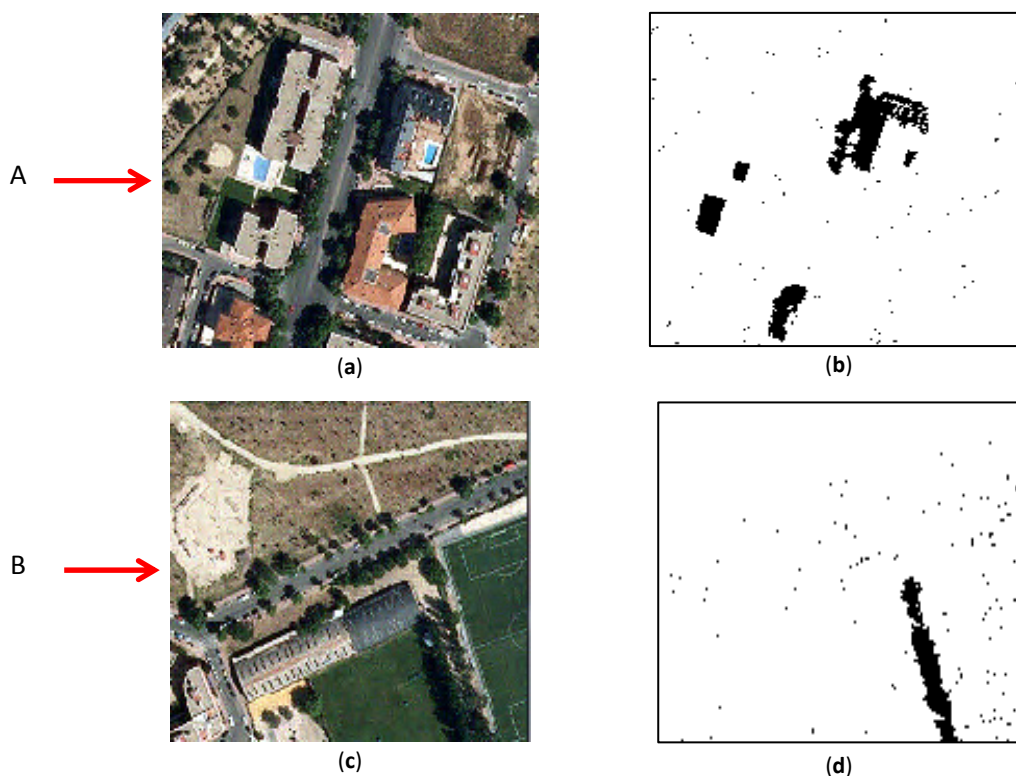

(a)

(b)

(c)

(d)

Figure 8. Spectral signatures of swimming pools and shadowed areas.

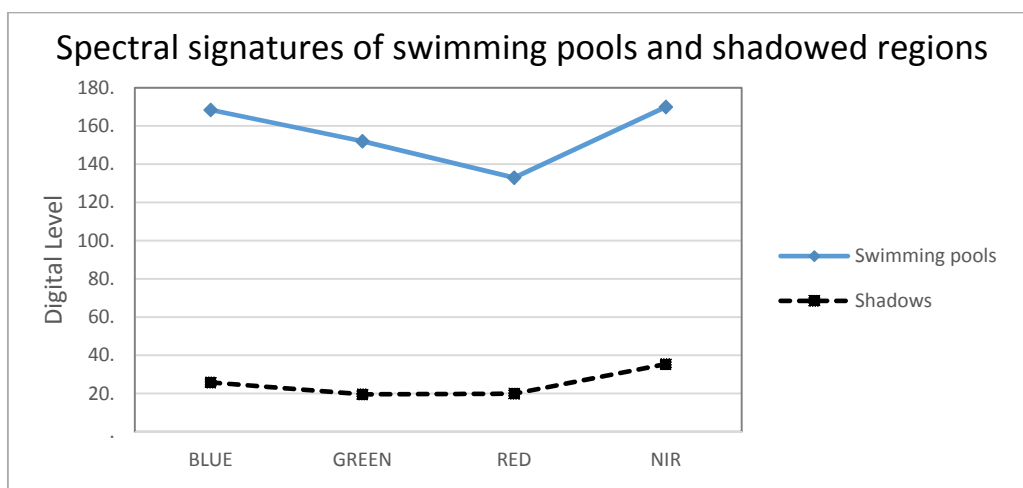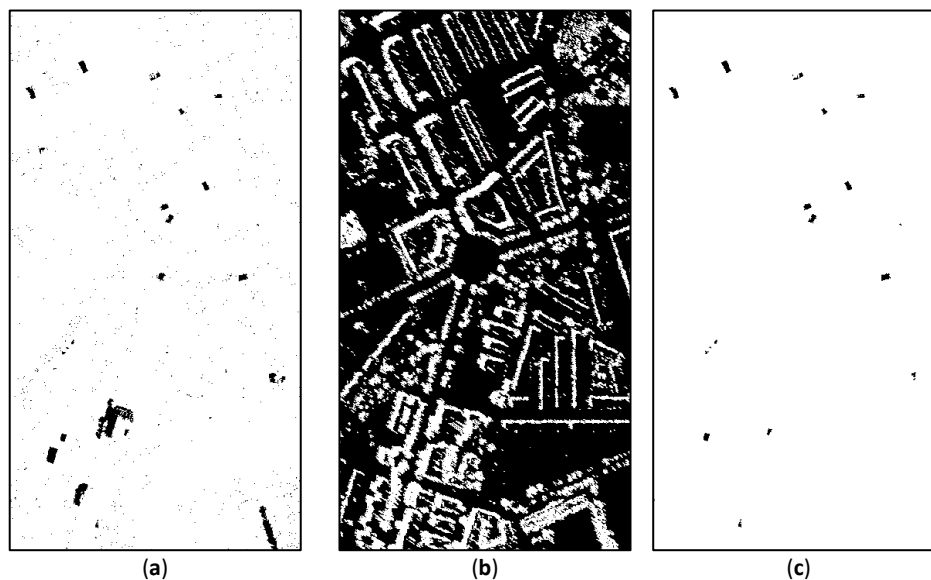**Figure 9.** (**a**) Swimming pools detected with false positives in shadowed areas; (**b**) shadowed regions in the studied area (white color represents shadowed areas, black shows no dark regions); and (**c**) swimming pools detected after removing false positives in shadowed regions.

(a) (b) (c)

3.7. Reference Data and Evaluation

Two supervised classifiers, Mahalanobis and SVM, and the proposed method of replacing the NDSPI with the NDWI were carried out and compared with the proposed method to test whether the proposed semi-automatic method provides better results than a supervised classification. In order to quantify the results obtained with each method, each result was compared with a ground truth elaborated by the authors (see Figure 1e). The black regions correspond to swimming pools (SP) and the white regions correspond to the background (BG). The evaluation was carried out to determine the confusion matrix [50], kappa index and commission and omission errors, comparing the ground truth with the result of each studied method.

4. Results and Discussion

The results obtained for the image in Figure 1a, which correspond to the area studied in the city of Alcalá de Henares, are shown below. Figure 10 shows the results obtained for each classification in Details A and B. Swimming pools are represented in black, and white color is used for the background.

Figure 10a–e shows the results of each method studied for the first 200 × 200 detail. Figure 10b shows the Mahalanobis classification results, in which false positives in shadowed areas have occurred. Figure 10c,e correspond with SVM and NDSPI methods, and in both images, it can be observed that swimming pools are determined without false positives or noise. Figure 10d shows the details for the NDWI method. It can be observed that not every swimming pool is detected, and furthermore, false positives are found in vegetated areas. Figure 10f–j represents the results of the second 200 × 200 detail for every method studied. Figure 10g,i represents the results of the Mahalanobis and NDWI methods. It can be observed that both methods provide false positives for

some buildings. Both methods consider these buildings as swimming pools due to their spectral responses. Figure 10h,j shows the best results obtained with the SVM and NDSPI methods. The detection provided by both methods is good, and swimming pools are properly determined. The SVM classifier provides some noise in isolated pixels, as seen in Figure 10h. In order to quantify the results obtained with every method, each result has been compared with a ground truth elaborated by the authors (see Figure 1e). Black regions correspond to swimming pools (SP) and white regions to the background (BG).

Figure 10. Results for two 200 × 200 details of the studied area are represented in (**a–e**) and (**f–j**), respectively. RGB images of both details are shown in (a) and (f), (b) and (g) present the results obtained with Mahalanobis classification, SVM detection is presented in (c) and (h), NDWI results are shown in (d) and (i), and the results provided by NDSPI are (e) and (j).
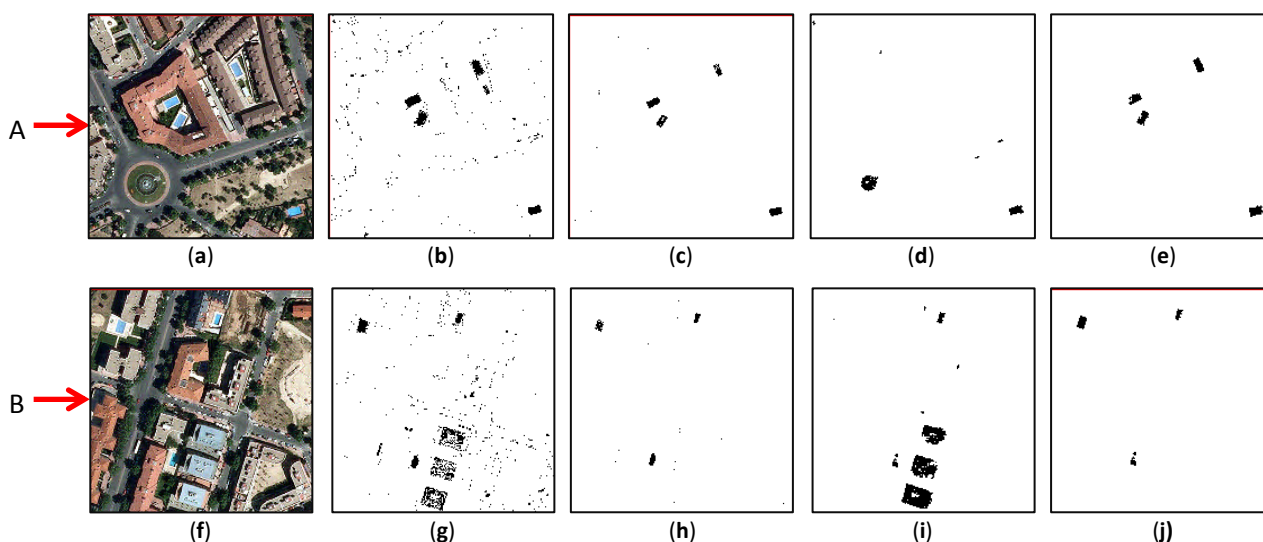

Table 1 shows the results provided by the studied methods. The Mahalanobis classifier provided lower accuracy (98.51%) than the SVM classifier (99.87%) did [51], due to labeling many of the pixels that belonged to the background as swimming pool. The kappa index of this method was also low, close to 0.3, and it produced a high commission error percentage in swimming pools and omission errors in the background, as more than 4000 background pixels were labeled as SP. However, only 90 SP pixels were incorrectly classified. This method provides a 91.53% producer's accuracy and 17.98% user's accuracy index [52]. The SVM classifier provided high accuracy, close to 99.9%, and its kappa index was 0.79. This means that the SVM supervised classification provides good results in swimming pool detection, as can be seen in the low commission/omission error rate. The highest percentage corresponded to SP omission error, as 312 SP pixels were incorrectly classified as background. The producer's and user's accuracy take values of 70.31% and 91.57%, respectively, for the SP category. The NDWI index provided high accuracy (close to 99.25%), but a low kappa index value, close to 0.19. It produced a high rate of commission and omission errors in the SP class: 781 SP pixels were labelled as BG, and 1468 BG pixels were classified as SP. In terms of producer's and user's accuracy, 25.69% and 15.54% are obtained, respectively. The results of the proposed method produced an accuracy of 99.86% and a kappa index close to 0.79. The commission and omission error

rates were similar to those obtained with the SVM classifier. The omission error in SP detection had the highest percentage, as 289 SP pixels were labeled as BG. The proposed method achieved a 72.5% producer's accuracy and 86.49% user's accuracy. According to these tables, the supervised SVM classification and the proposed method with the NDSPI index are the best methods. Both provide almost the same results, with accuracy close to 99.9% and a kappa index of 0.79.

Table 1. Confusion matrix of the studied methods, where columns are the ground truth and rows represent the classification results. SP, swimming pools; BG, background.

	MAHALANOBIS			SVM			NDWI			NDSPI		
	SP	BG	Σ	SP	BG	Σ	SP	BG	Σ	SP	BG	Σ
SP	962	4387	5349	739	68	807	270	1468	1738	762	119	881
BG	89	294,387	294,476	312	298,706	299,018	781	297,306	298,087	289	298,655	298,944
Σ	1051	298,774	299,825	1051	298,774	299,825	1051	298,774	299,825	1051	298,774	299,825
	(295,349/299,825) 98.51%			(299,445/299,825) 99.87%			(27,576/299,825) 99.25%			(299,417/299,825) 99.86%		
	Kappa coefficient = 0.2965			**Kappa coefficient = 0.7949**			**Kappa coefficient = 0.1901**			**Kappa coefficient = 0.7881**		
	Commission	**Omission**		**Commission**	**Omission**		**Commission**	**Omission**		**Commission**	**Omission**	
SP	82.02%	8.47%		8.43%	29.69%		84.46%	74.31%		13.51%	27.50%	
BG	0.03%	1.47%		0.10%	0.02%		0.26%	0.49%		0.10%	0.04%	
	Prod. Acc.	**User Acc.**		**Prod. Acc.**	**User Acc.**		**Prod. Acc.**	**User Acc.**		**Prod. Acc.**	**User Acc.**	
SP	91.53%	17.98%		70.31%	91.57%		25.69%	15.54%		72.50%	86.49%	
BG	98.53%	99.97%		99.98%	99.90%		99.51%	99.74%		99.96%	99.90%	

5. Conclusions

Efficient methods to detect sheets of water automatically could be of vital importance for firefighting. In this paper, we propose a novel method for the semi-automatic detection of swimming pools in urban environments from aerial images and LIDAR data. The proposed method uses the NDSPI based on the spectral response of swimming pools, a region adjacency graph, and Dempster–Shafer theory to successfully identify the location of this cover in urban areas. The behavior of the proposed method was discussed in conjunction with three other methods to detect swimming pools: two supervised classifications (Mahalanobis and SVM) and the proposed method for detecting pools using the NDWI, which is useful in the detection of large bodies of water. The performance of the four methods was tested in a real dataset from the Spanish city of Alcalá de Henares. The creation of a ground truth of the studied region enabled numerical analysis of accuracy and determination of the kappa coefficient for the different methods.

The results show the performance of each method conducted on the studied dataset. Through a visual analysis, it can be seen that the proposed method using the NDSPI and SVM classifier produced the best results in the studied region.

The proposed method using the NDSPI achieved an accuracy of 99.86% and a kappa index of 0.79, better than the accuracy obtained with the Mahalanobis classification and proposed method with the NDWI (90.19% and 99.25%, respectively) and close to the 99.87% accuracy and 0.79 kappa index produced by the SVM supervised classification. It can be observed that almost every swimming pool was detected by the SVM classifier and proposed method. Although false positives were found with

some covers, commission errors were quite lower than in other methods, such as the Mahalanobis classifier. The main innovation of the proposed method is that it does not require prior training, as do supervised classifiers, and it only needs the correct threshold of every decision index used in the method to obtain good detection of swimming pools.

There are different types of water body land covers, such as oceans, seas and rivers, and there is no single best method or index to detect land covers in all cases, because the results vary by the spectral and spatial properties of each type of land cover. According to the results obtained, we can conclude that the method presented in this paper is useful in the semi-automatically determining of the location of swimming pools in urban areas from aerial images and LIDAR data.

Acknowledgments

Author Contributions

Both authors, B. Rodríguez-Cuenca and M.C. Alonso, designed the research, performed data analysis, and contributed with ideas, writing and discussion.

Conflicts of Interest

The authors declare no conflict of interest.

References

1. Holmes, W.S.; Buffalo, N.Y. Automatic photointerpretation and target location. *Proc. IEEE* **1966**, *54*, 1679–1686.
2. Voirin, Y.; Benie, G.B.; Deng-Chen, H.; Ko, F.; Goita, K. A Forest Map Updating Expert System Based on the Integration of Low Level Image Analysis and Photointerpretation Techniques. In Proceedings of 2002 IEEE International Geoscience and Remote Sensing Symposium (IGARSS), Toronto, ON, Canada, 24–28 June 2002; pp. 1618–1620.
3. Richards, J.A.; Jia, X. *Remote Sensing Digital Image Analysis*; Springer Verlag: New York, NY, USA, 2006.
4. Cristianini, N.; Shawe-Taylor, J. *An Introduction to Support Vector Machines and Other Kernel-Based Learning Methods*; Cambridge University Press: Cambridge, UK, 2000.
5. Cortes, C.; Vapnik, V. Support-vector networks. *Machine Learn.* **1995**, *20*, 273–297.
6. Bischof, H.; Schneider, W.; Pinz, A.J. Multispectral classification of Landsat-images using neural networks. *IEEE Trans. Geosci. Remote Sens.* **1992**, *30*, 482–490.
7. Gath, I.; Geva, A.B. Unsupervised optimal fuzzy clustering. *IEEE Trans. Pattern Anal. Machine Intell.* **1989**, *11*, 773–780.

8. Duda, T.; Canty, M.; Klaus, D. Unsupervised Land-Use Classification of Multispectral Satellite Images. A Comparison of Conventional and Fuzzy-Logic Based Clustering Algorithms. In Proceedings of 1999 IEEE International Geoscience and Remote Sensing Symposium (IGARSS), Hamburg, Germany, 28 June–02 July 1999; pp. 1256–1258.

9. Adams, J.B.; Sabol, D.E.; Kapos, V.; Almeida Filho, R.; Roberts, D.A.; Smith, M.O.; Gillespie, A.R. Classification of multispectral images based on fractions of endmembers: Application to land-cover change in the Brazilian Amazon. *Remote Sens. Environ.* **1995**, *52*, 137–154.

10. Song, J.H.; Han, S.H.; Yu, K.Y.; Kim, Y.I. Assessing the Possibility of Land-Cover Classification Using LIDAR Intensity Data. In Proceedings of ISPRS Commission III Symposium, Graz, Austria, 9–13 September 2002.

11. Antonarakis, A.S.; Richards, K.S.; Brasington, J. Object-based land cover classification using airborne LiDAR. *Remote Sens. Environ.* **2008**, *112*, 2988–2998.

12. Charaniya, A.P.; Manduchi, R.; Lodha, S.K. Supervised Parametric Classification of Aerial LiDAR Data. In Proceedings of 2004 Conference on Computer Vision and Pattern Recognition Workshop, Washington, DC, USA, 27 June–2 July 2004.

13. Rottensteiner, F.; Briese, C. Automatic Generation of Building Models from LIDAR Data and the Integration of Aerial Images. In Proceedings of ISPRS Working Group III/3 Workshop on "3-D Reconstruction from Airborne Laserscanner and InSAR Data", Dresden, Germany, 8–10 October 2003.

14. Fitzsimmons, B.; Buck, H. Automatic swimming pool identification for fire suppresion. *Proc. SPIE* **2012**, *8515*, doi:10.1117/12.927774.

15. Tien, D.; Rudra, T.; Hope, A.B. Swimming Pool Identification from Digital Sensor Imagery Using SVM. In Proceedings of 9th Biennial Conference of the Australian Pattern Recognition Society on Digital Image Computing Techniques and Applications, Glenelg, Australia, 3–5 December 2007; pp. 523–527.

16. McFeeters, S. Using the Normalized Difference Water Index (NDWI) within a geographic information system to detect swimming pools for mosquito abatement: A practical approach. *Remote Sens.* **2013**, *5*, 3544–3561.

17. Gao, B. NDWI—A normalized difference water index for remote sensing of vegetation liquid water from space. *Remote Sens. Environ.* **1996**, *58*, 257–266.

18. Xu, H. Modification of Normalised Difference Water Index (NDWI) to enhance open water features in remotely sensed imagery. *Int. J. Remote Sens.* **2006**, *27*, 3025–3033.

19. Zhang, Z.; Prinet, V.; Ma, S. Water Body Extraction from Multi-Source Satellite Images. In Proceedings of 2003 IEEE International Geoscience and Remote Sensing Symposium (IGARSS), Toulouse, France, 21–25 July 2003; pp 3970–3972.

20. Frazier, P.S.; Page, K.J. Water body detection and delineation with Landsat TM data. *Photogramm. Eng. Remote Sens.* **2000**, *66*, 1461–1467.

21. Silveira, M.; Heleno, S. Separation between water and land in SAR images using region-based level sets. *IEEE Geosci. Remote Sens. Lett.* **2009**, *6*, 471–475.

22. Henry, J.B.; Chastanet, P.; Fellah, K.; Desnos, Y.L. Envisat multi-polarized ASAR data for flood mapping. *Int. J. Remote Sens.* **2006**, *27*, 1921–1929.

23. Liu, H.; Jezek, K.C. A complete high-resolution coastline of antarctica extracted from orthorectified radarsat SAR imagery. *Photogramm. Eng. Remote Sens.* **2004**, *70*, 605–616.

24. Niedermeier, A.; Hoja, D.; Lehner, S. Topography and morphodynamics in the German Bight using SAR and optical remote sensing data. *Ocean Dyn.* **2005**, *55*, 100–109.

25. Galindo, C.; Moreno, P.; Gonzalez, J.; Arevalo, V. Swimming Pools Localization in Colour High-Resolution Satellite Images. In Proceedings of 2009 IEEE International Geoscience and Remote Sensing Symposium (IGARSS), Cape Town, South Africa, 12–17 July 2009; pp. IV-510–IV-513.

26. Myint, S.; Gober, P.; Brazel, A.; Grossman-Clarke, S.; Weng, Q. Per-pixel *vs.* object-based classification of urban land cover extraction using high spatial resolution imagery. *Remote Sens. Environ.* **2011**, *115*, 1145–1161.

27. Raber, G.T.; Jensen, J.R.; Schill, S.R.; Schuckman, K. Creation of digital terrain models using an adaptive lidar vegetation point removal process. *Photogramm. Eng. Remote Sens.* **2002**, *68*, 1307–1315.

28. Streutker, D.R.; Glenn, N.F. LiDAR measurement of sagebrush steppe vegetation heights. *Remote Sens. Environ.* **2006**, *102*, 135–145.

29. De Agirre, A.M.; Malpica, J.A. Constructing a Digital Terrain Model from LiDAR Data. In *Advances in Geoinformation Technologies*; Horak, J., Halounova, L., Hlasny, T., Kusendova, D., Vozenilek, V., Eds.; Institute of Geoinformatics: Ostrava, Czech Republic, 2010; pp. 47–59.

30. Wu, Z.; Leahy, R. An optimal graph theoretic approach to data clustering: Theory and its application to image segmentation. *IEEE Trans. Pattern Anal. Machine Intell.* **1993**, *15*, 1101–1113.

31. Haralick, R.M.; Shapiro, L.G. Image segmentation techniques. *Comput. Vis. Graph. Image Process.* **1985**, *29*, 100–132.

32. Bins, L.S.; Fonseca, L.M.G.; Erthal, G.J.; Li, F.M. Satellite Imagery Segmentation: A Region Growing Approach. In Proceedings of VIII Brazilian Symposium on Remote Sensing, Salvador, Brazil, 14–19 April 1996; pp. 677–680.

33. Yu Jin, Z. A Review of Recent Evaluation Methods for Image Segmentation. In Proceedings of Sixth International Symposium on Signal Processing and its Applications, Kuala Lumpur, Malaysia, 13–16 August 2001; pp. 148–151.

34. Rodriguez-Cuenca, B.; Malpica, J.A.; Alonso, M.C. Region-Growing Segmentation of Multispectral High-Resolution Space Images with Open Software. In Proceedings of 2012 IEEE International Geoscience and Remote Sensing Symposium (IGARSS), Munich, Germany, 22–27 July 2012; pp. 4311–4314.

35. Mehnert, A.; Jackway, P. An improved seeded region growing algorithm. *Pattern Recognit. Lett.* **1997**, *18*, 1065–1071.

36. Fan, J.; Zeng, G.; Body, M.; Hacid, M.-S. Seeded region growing: An extensive and comparative study. *Pattern Recognit. Lett.* **2005**, *26*, 1139–1156.

37. Sulaiman, S.N.; Isa, N.A.M. Adaptive fuzzy-K-means clustering algorithm for image segmentation. *IEEE Trans. Consum. Electron.* **2010**, *56*, 2661–2668.

38. Gutman, G. Monitoring Global Vegetation Using AVHRR. In Proceedings of 1998 IEEE International Geoscience and Remote Sensing Symposium (IGARSS), Seattle, WA, USA, 6–10 July 1998; pp. 2509–2511.

39. Schneider, S.R.; McGinnis, D.F. The NOAA AVHRR: A New Sensor for Monitoring Crop Growth. In Proceedings of the 8th International Machine Processing of Remotely Sensed Data Symposium, West Lafayette, IN, USA, 27–29 June 1982; pp. 281–290.

40. Malingreau, J.P.; Tucker, C.J. The Contribution of AVHRR Data for Measuring and Understanding Global Processes: Large Scale Deforstation in the Amazon Basin. In Proceedings of 1987 IEEE International Geoscience and Remote Sensing Symposium (IGARSS), New York, NY, USA, 18–21 May 1987; pp. 484–489.

41. Clode, S.; Kootsookos, P.J.; Rottensteiner, F. The automatic extraction of roads from LIDAR data. *Int. Arch. Photogramm. Remote Sens. Spat. Inf. Sci.* **2004**, *XXXVIII*, 231–236.

42. Qiao, C.; Luo, J.; Sheng, Y.; Shen, Z.; Zhu, Z.; Ming, D. An adaptive water extraction method from remote sensing image based on NDWI. *Indian Soc Remote Sens.* **2012**, *40*, 421–433.

43. Dempster, A.P. A generalization of Bayesian Inference. *J. Royal Stat. Soc. Series B Methodol.* **1968**, *30*, 205–247.

44. Shafer, G. *A Mathematical Theory of Evidence*; Princeton University Press: Princeton, NJ, USA, 1976.

45. Zarco, I.A.; Rodríguez, C.A.; Sendra, J.B.; Malpica, J.A.; Martín-Loeches, M.; Asensio, E.P.; Vela, J.T. Un procedimiento para elaborar mapas de riesgos naturales aplicado a Honduras. In *Anales de Geografía*; Universidad Complutense: Madrid, Spain, 2003; pp. 55–73.

46. Yen, J. Generalizing the Dempster-Schafer theory to fuzzy sets. *IEEE Trans. Syst. Man Cybern.* **1990**, *20*, 559–570.

47. Zadeh, L.A. Fuzzy sets. *Inf. Control* **1965**, *8*, 338–353.

48. Malpica, J.A.; Alonso, M.C.; Sanz, M.A. Dempster–Shafer theory in geographic information systems: A survey. *Expert Syst. Appl.* **2007**, *32*, 47–55.

49. De Agirre, A.M.; Malpica, J.A. Detecting Shadows in a Segmented Land Use Land Cover Image with LIDAR Data. In Proceedings of 2012 IEEE International Geoscience and Remote Sensing Symposium (IGARSS), Munich, Germany, 22–27 July 2012; pp. 5458–5461.

50. Jensen, J.R. *Introductory Digital Image Processing*; Prentice-Hall: New York, NY, USA, 1996.

51. Gigandet, X.; Cuadra, M.B.; Pointet, A.; Cammoun, L.; Caloz, R.; Thiran, J.P. Region-Based Satellite Image Classification: Method and Validation. In Proceedings of 2005 IEEE International Conference on Image Processing (ICIP), Genoa, Italy, 11–14 September 2005; doi:10.1109/ICIP.2005.1530521.

52. Congalton, R.G. Accuracy assessment and validation of remotely sensed and other spatial information. *Int. J. Wildland Fire* **2001**, *10*, 321–328.